The Meteoritical Society

Meteoritics & Planetary Science 56, Nr 9, 1652–1668 (2021)
doi: 10.1111/maps.13729

Salt grains in hypervelocity impacts in the laboratory: Methods to sample plumes from the ice worlds Enceladus and Europa

C. R. FISHER, M. C. PRICE, and M. J. BURCHELL *

Centre for Astrophysics and Planetary Science, School of Physical Sciences, University of Kent, Canterbury, Kent CT2 7NH, UK
*Corresponding author. E-mail: m.j.burchell@kent.ac.uk

(Received 11 March 2021; Revised 05, July 2021; revision accepted 17 July 2021)

Abstract–The plumes naturally erupting from the icy satellite Enceladus were sampled by the Cassini spacecraft in high-speed fly-bys, which gave evidence of salt. This raises the question of how salt behaves under high-speed impact, and how it can best be sampled in future missions to such plumes. We present the results of 35 impacts onto aluminum targets by a variety of salts (NaCl, $NaHCO_3$, $MgSO_4$, and $MgSO_4{\cdot}7H_2O$) at speeds from 0.26 to 7.3 km s^{-1}. Using SEM-EDX, identifiable projectile residue was found in craters at all speeds. It was possible to distinguish NaCl and $NaHCO_3$ from each other, and from the magnesium sulfates, but not to separate the hydrous from anhydrous magnesium sulfates. Raman spectroscopy on the magnesium sulfates and $NaHCO_3$ residues failed to find a signal at low impact speeds (<0.5 km s^{-1}) where there was insufficient projectile material deposited at the impact sites. At intermediate speeds (0.5 to 2–3 km s^{-1}), identifiable Raman spectra were found in the impact craters, but not at higher impact speeds, indicating a loss of structure during the high speed impacts. Thus, intact capture of identifiable salt residues on solid metal surfaces requires impact speeds between 0.75 and 2 km s^{-1}.

INTRODUCTION

Subsurface oceans are now believed to exist on several icy satellites and bodies in the outer solar system. The first reports concerning oceans on Europa and Callisto (Carr et al. 1998; Khurana et al. 1998; Pappalardo et al. 1999) have been followed by further reports including observations concerning Enceladus (Dougherty et al. 2006). In the case of Enceladus, tidal effects combined with internal heating have created what appears to be a natural eruption of water through the ice in the form of plumes (e.g., Hansen et al. 2006; Porco et al. 2006; Waite et al. 2006; Nimmo et al. 2007). There is some evidence that Europa may have similar plumes (e.g., Roth et al. 2014; Sparks et al. 2016). The role of oceans as potential host sites for life means these bodies are the object of significant attention and speculation (e.g., see Hendrix et al. [2019] and references therein).

That the oceans are brine rich (e.g., see Sohl et al. [2010], or Grasset et al. [2017], for a discussion of the nature of the oceans) implies that the plumes may also contain salts. Indeed, the Cassini space mission detected dust grains when passing close to Enceladus in 2005 (Spahn et al. 2006), and later analysis identified salt (NaCl via signals for sodium and potassium)-rich grains (Postberg et al. 2009, 2011). Indeed, it is also suggested that the Europan ocean is rich in NaCl (Hand and Carlson 2015). Hydrated magnesium sulfate salts are also present, and epsomite ($MgSO_4{\cdot}7H_2O$) has been suggested to be present on the surface of Europa, for example, as a radiation product (Brown and Hand 2013).

Models of plume emission suggest that as much as 1600 μg of material (grain size 0.01–10 μm) can be intercepted per m^2 of collector, in a single pass through the Enceladus plume at 25 km altitude (Guzman et al. 2019). As well as salt, the Cassini mission has reported the presence of organic materials in the Enceladus plumes (Postberg et al. 2018; Khawaja et al. 2019), detected, like the original NaCl (Postberg et al. 2009, 2011), in the cosmic dust analyzer (Srama et al. 2004). This instrument used impact ionization to produce ionic plasmas, whose contents are then probed via time-of-flight mass spectroscopy. At Europa, larger grains may be found in the plume, with grains a few 10s of microns

in size predicted up to altitudes of 200 km (see Lorenz 2016).

The collection of grains from plumes emerging from Enceladus, or Europa, will involve a high-speed impact. The impact speed will either be the orbital speed around the icy satellite (a function of altitude and mass of the central body, which for Enceladus ranges between 100 and 200 m s^{-1} at low altitudes, versus 1–2 km s^{-1} at Europa, see Traspas and Burchell 2021), or the fly-by speed of the spacecraft (which for Cassini at Enceladus produced impacts ranging from some 4.5 to 15 km s^{-1}, see Khawaja et al. 2019). Studies such as Tsou et al. (2012) suggest that to sample the organic contents of the Enceladan plumes, fly-by speeds should be kept at speeds as low as 3.0–4.5 km s^{-1}. Impact speeds in future such missions may thus range from a few hundreds of m s^{-1} to, say, 5 km s^{-1}. The transition from normal speed impact to hypervelocity (km s^{-1} regime) impact cratering has long been studied, for example, see Bernard and Hörz (1995), who studied impacts of 3.2 mm diameter glass spheres onto aluminum 1100 at speeds of 0.7–7 km s^{-1}. The evolution of the projectile residue with impact speed, including onset of melting at around 2–4 km s^{-1}, was also reported by Bernard and Hörz (1995).

Various types of missions and instrument packages have been suggested for future space missions to bodies such as Enceladus (e.g., Mathies et al. 2017) and Europa (e.g., Southworth et al. 2015), which would analyze the plumes. Much interest has focused on the viability of methods for intact or semi-intact capture of long-chain organics in the plumes during hypervelocity flybys (e.g., see Burchell and Harriss 2020; New et al. 2020a, 2020b; Kazemi et al. 2021). This builds on work which aims to understand in the laboratory how to interpret the time-of-flight impact ionization spectra of organics (e.g., Goldsworthy et al. 2002, 2003; Burchell and Armes 2011; Chan et al. 2021). Even the possibility of collecting life forms themselves in fly-bys has been considered (Traspas and Burchell 2021). It is clearly of interest to collect relatively intact fragments, rather than just time-of-flight mass spectra.

However, there is a more basic question to ask before considering the organics in a plume, namely what can be said about the salt content itself? If the droplets in the plume are intercepted by a passing spacecraft, can the nature of the salt be determined despite the high-speed impact?

Accordingly, we present herein a laboratory study of high-speed impacts of salt grains, using a two-stage light gas gun firing projectiles at aluminum targets (a typical collection substrate used by, among others, Burchell and Harriss [2020]; New et al. [2020a, 2020b], etc.). Impact speeds ranged from 0.26 to 7.34 km s^{-1} and grain sizes varied from 10 μm up to 90 μm. Four types of salt were used: sodium chloride (NaCl, melting temperature 1074 K), sodium bicarbonate ($NaHCO_3$, thermal decomposition temperature 353 K) and magnesium sulfate ($MgSO_4$), with the magnesium sulfate in both hydrous (epsomite, $MgSO_4{\cdot}7H_2O$) and anhydrous forms. The anhydrous and hydrous forms of magnesium sulfate not only have different densities (2.66 and 1.67 g cm^{-3}, respectively) but also very different decomposition temperatures (1379 and 298 K, respectively) providing good benchmarks for projectile survival. The types of salt used thus included two containing sodium, namely halite (NaCl), and sodium bicarbonate ($NaHCO_3$), as well magnesium sulfate, found in water or evaporates on Earth and elsewhere, and used here in both its anhydrous form ($MgSO_4$) and a hydrated form (epsomite, $MgSO_4{\cdot}7H_2O$). Analysis techniques were SEM-EDX (elemental identification) and Raman spectroscopy (based on bonding in the materials).

Raman spectroscopy has long been used to identify materials including minerals via their bonding structure. While it does not work on all materials (only if they are polarizable), it does work on a wide range of minerals and organics. Recently, the NASA Mars 2020 rover has carried a Raman spectrometer to Mars (e.g., Wiens et al. 2021) and the ESA ExoMars 2022 rover will do the same (Moral et al. 2020). More significantly, impact residues in craters in aluminum foil samples returned to Earth by the NASA Stardust mission to comet 81P/Wild-2 (Brownlee et al. 2006) have been analyzed using Raman spectroscopy (e.g., Bridges et al. 2010; Foster et al. 2013). This was after it was shown that many minerals gave Raman signals from residues in craters after impacts on aluminum at the Stardust cometary encounter speed of 6.1 km s^{-1} (Burchell et al. 2008). The survival of intact organics in impact crater residues is less certain. Analysis of space-exposed aluminum surfaces combined with laboratory experiments showed melted (and in some cases, only partially melted) residues lining impact craters (e.g., Bunch et al. 1991; Berthoud et al. 1995), with assignments of possible origins being made based on the presence of various combinations of elements. More promisingly, New et al. (2020a) have shown recognizable Raman spectra from PMMA in residues in impacts on indium targets at 2–3 km s^{-1}. However, Burchell and Harriss (2020) showed that at least some organics (polystyrene and PMMA) do not provide Raman signals after impacts on aluminum at 5–6 km s^{-1} suggesting that thermal decomposition can occur for at least some materials during impacts at a few km s^{-1}. Thus, whether samples collected from ice-world plumes are to be analyzed in situ, or after a return to Earth, it is of interest to determine how

different salts (with various thermal decomposition temperatures) will respond to Raman analysis after capture at high speed.

METHOD

The Kent two-stage light gas gun was used in this work (Burchell et al. 1999). The gun was originally optimized to fire at speeds above 1 km s^{-1}, but has recently been adjusted to also permit lower speeds down to around 250 m s^{-1} (Hibbert et al. 2017). This permits a wide range of speeds to be achieved in a single facility. The projectiles are launched in a discardable sabot fired from a rifled barrel. After the sabot is separated, the projectiles proceed to the target located in a vacuum chamber at a typical pressure of 0.5 mbar. The projectile speed was measured in each shoot to typically within a few percent. In this work, the projectiles in each shot were multiple grains of salt fired as a buckshot. Only one salt type was used per shot.

The grains were prepared by grinding larger samples and then sieving. The selected size range from the sieving was 75–90 μm. Images of the projectiles are shown in Fig. 1. The targets used were sheets of aluminum foil (type 1080). Note that in previous impact cratering work, for example, New et al. (2020a), a slightly different aluminum alloy has often been used (Al 1100). Both these 1000 series aluminum alloys are >99% pure and have similar densities (2700 and 2710 kg m^{-3}, respectively). After each shot, the target foil was examined first under an optical microscope to confirm the presence of impact craters, and then in a SEM. The SEM was a Hitachi S-3400N with an Oxford XMax-80 detector for EDX measurements. Raman spectroscopy was then performed on the craters. The Raman spectrometer was a Horiba LabRam HR spectrometer, with 600 lines per mm grating spacing giving an approximately 2 cm^{-1} wave number resolution, and an integral Olympus BX41 optical microscope (1–2 μm spatial resolution on the target). A 785 nm laser was used for the Raman illumination.

Impact shock pressures were found in two ways. The first was by use of the planar impact approximation (PIA), which uses a linear wave speed equation for each material in the impact to obtain a peak shock pressure (see Melosh [2013] for a discussion). The linear shock wave speed relation for the materials involved is of the form:

$$U = c + su, \tag{1}$$

where u is particle velocity, U is the shock velocity, and c and s are found experimentally. Separate wave speed relations hold for the projectile and target materials and hence separate values of c and s are required. For NaCl, we use $c = 3.477$ km s^{-1} and $s = 1.336$ (with density = 2163 kg m^{-3}), while for the aluminum foil target we use the data for Al1100 where $c = 5.376$ km s^{-1}, $s = 1.339$, and density = 2712 kg m^{-3} (all data taken from Marsh 1980). Using these values, the PIA gives an estimate of peak shock pressure close to the impact plane. Although the linear wave speed data are for a slightly different grade of aluminum alloy to that used here, no data are available for Al1080. To test if this has biased our results, we have varied the aluminum density used in the PIA calculations and also used data for a different grade of aluminum (see table 3.1, Melosh 2013). In each case, the resulting peak shock pressures vary by <1%.

While giving a representative peak value for the shock pressure in a sample, the PIA does not, however, allow for the finite size of samples, or how the peak pressure may vary across a projectile. To understand this better, a 3-D hydrocode simulation was run, using the Autodyn code (see Hayhurst and Clegg 1987) for the impacts of halite onto aluminum using shock data from Fritz et al. (1971). Individual tracer points across the projectile allowed the peak shock pressure to be found at discrete positions in the projectile.

In both the PIA and Autodyn cases, shock Hugoniot data are required. However, while this is available for NaCl, it is not available for the other salts used here. Therefore, we only show results for shock pressures for NaCl in this article.

RESULTS

Thirty-five shots were performed. There were 10 shots each with NaCl and $MgSO_4$, 8 with $MgSO_4 \cdot 7H_2O$, and 7 with $NaHCO_3$ projectiles. The impact speeds ranged from 0.26 to 7.34 km s^{-1} (see Table 1). All impacts were at normal incidence.

Crater Morphology

Typical crater images are shown in Figs. 2–5. With each salt type, an evolution in crater shape can be seen as impact speed increases (Table 2). At low speeds, there is little sign of cratering, instead indentations are found in the target foil. It thus appears that low-speed impacts cause the impactor to rebound, leaving only small amounts of material at the impact site. This behavior has been seen before. In a separate study of organic projectiles (4–10 μm diameter) impacting metal foils at speeds of 0.5–3 km s^{-1}, similar behavior including rebound of the projectiles was seen in various

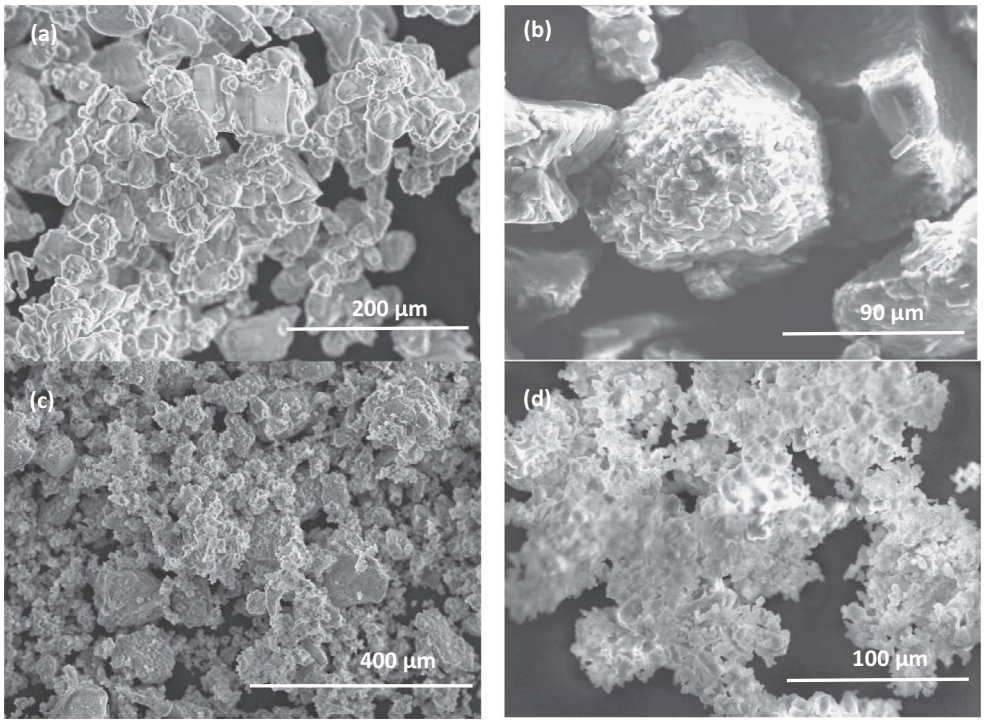

Fig. 1. SEM images showing examples of each projectile type: (a) sodium chloride, (b) sodium bicarbonate, (c) hydrous magnesium sulfate (epsomite), and (d) anhydrous magnesium sulfate.

Table 1. Shot parameters.

Projectile	Speed (km s^{-1})	Projectile	Speed (km s^{-1})	Projectile	Speed (km s^{-1})	Projectile	Speed (km s^{-1})
NaCl	0.329	$NaHCO_3$	0.261	$MgSO_4$	0.316	$MgSO_4 \cdot H_2O$	0.288
	0.486		0.499		0.374		0.638
	0.954		0.931		0.623		0.891
	1.94		1.98		0.937		2.06
	2.19		3.28		1.99		2.11
	2.23		4.92		3.23		3.29
	3.57		6.94		5.14		5.14
	4.73				5.32		7.04
	5.03				6.42		
	6.67				7.34		

scenarios involving certain types of projectile and target materials, and the lowest speeds (New et al. 2020a).

In some cases, at around 0.5–1 km s^{-1}, broken projectile fragments can be seen in the indentations/craters, and very occasionally even intact grains were found partially embedded in the foil. Above 1 km s^{-1}, there is evidence of craters with raised rims with initially thin lips. Then as speed increases above 2–3 km s^{-1}, the craters become the traditional turned over, broad-rimmed hypervelocity craters. The appearance of large amounts of recognizable impactor fragments in the craters falls as the impact speeds exceed a few km s^{-1}, with more melted residue appearing.

Peak Pressures

Using the impact speeds in Table 1, the PIA was used to give estimates of peak shock pressures in halite (Table 3). In addition, Autodyn modeling for a spherical 60 µm diameter halite projectile impact on aluminum at a range of impact speeds produced the results shown in Table 3. Peak pressures were taken from gauges placed at the front (which strikes the target), middle, and rear of the projectile. The gauges close to the contact point show peak shock pressures very similar to those from the PIA (see Table 3). As expected, the peak shock pressures fall across the

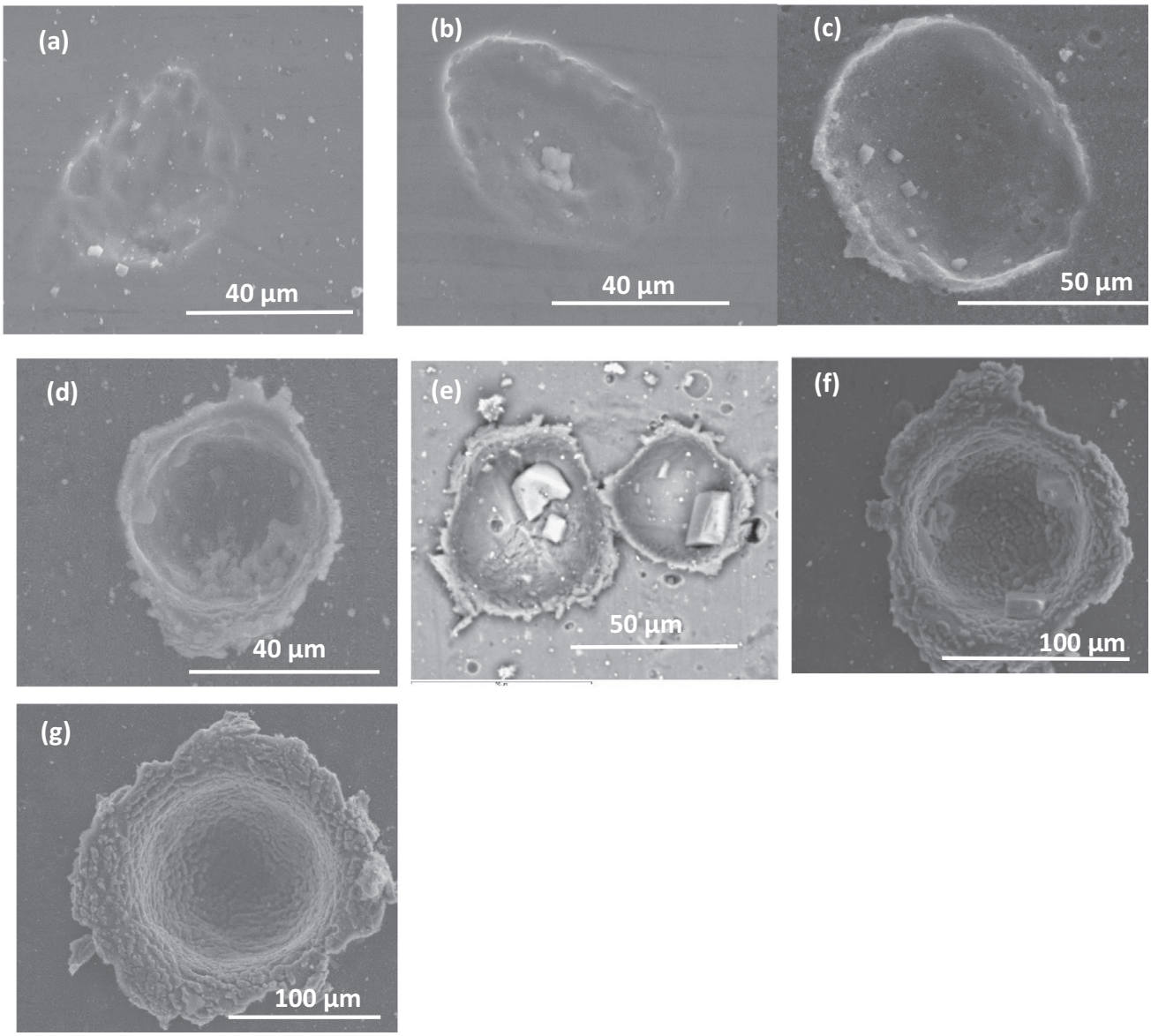

Fig. 2. SEM images showing example impact craters (NaCl): (a) 0.329 km s^{-1}, (b) 0.486 km s^{-1}, (c) 0.954 km s^{-1}, (d) 1.94 km s^{-1}, (e) 3.57 km s^{-1}, (f) 4.73 km s^{-1}, (g) 6.67 km s^{-1}.

interior of the projectile, with relatively low pressures at the less shocked rear. Indeed, at low speeds (<1 km s^{-1}), the rear of the projectile does not appear to suffer any significant shock. That is, the front of the projectile near the contact zone experiences the maximum shock, and the rear is left relatively unshocked due to the free rear surface.

Compositional Analysis: SEM-EDX

To confirm that the craters were indeed the result of impacts by salt grains, SEM-EDX spectra were obtained. Background spectra for the foil itself were regularly obtained when searching for craters, and showed the expected strong Al peak, along with very small peaks at just above 0 and 3 keV (the latter being an interference peak caused by the aluminum). On occasion, iron contamination was found on the foils, which comes from inclusions in the foil.

Typical spectra from the raw grains are shown in Fig. 6. The spectra for NaCl and $NaHCO_3$ are clearly distinct from those for the magnesium sulfates (also see Table 4). However, $MgSO_4$ and $MgSO_4 \cdot 7H_2O$ show the same elemental lines and only differ in the intensity of the oxygen peak. Although indicative, the EDX spectra alone cannot determine the precise nature of a

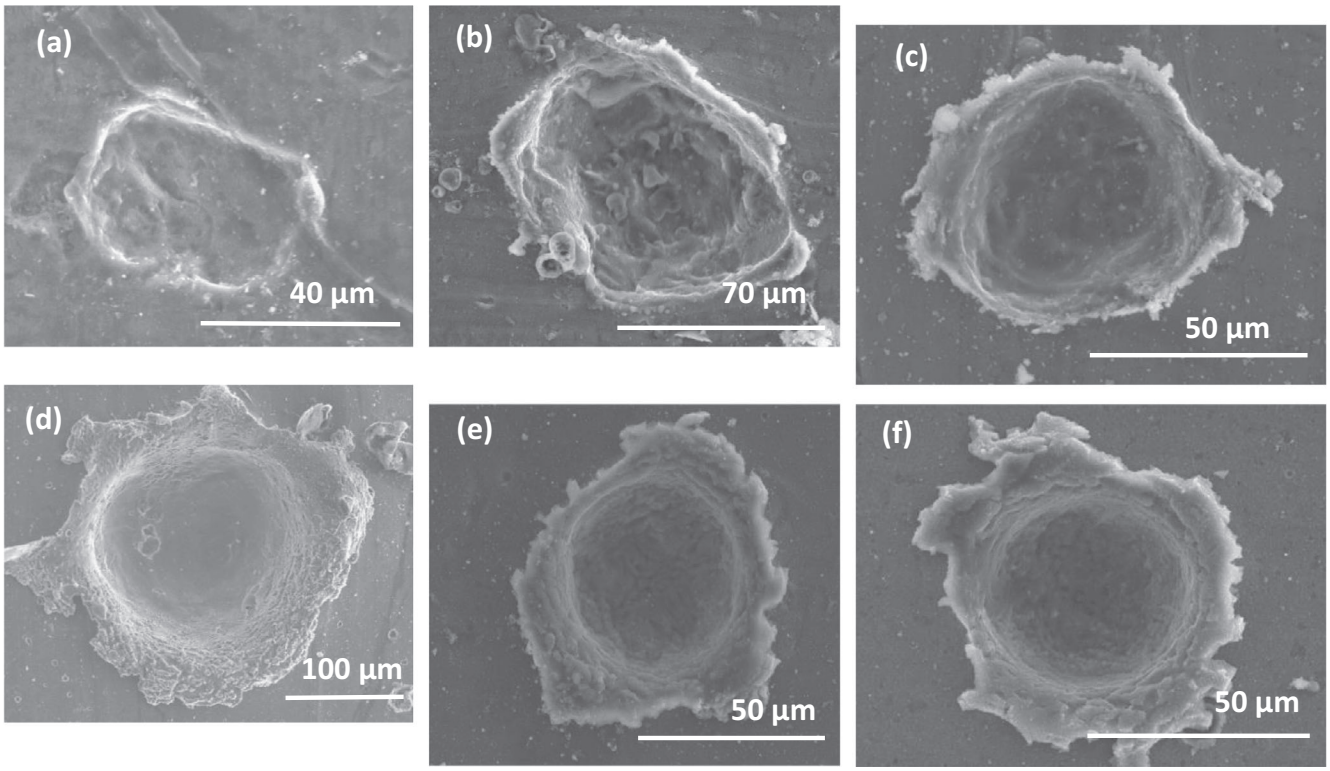

Fig. 3. SEM images showing example impact craters ($NaHCO_3$): (a) 0.499 km s^{-1}, (b) 0.931 km s^{-1}, (c) 1.93 km s^{-1}, (d) 3.28 km s^{-1}, (e) 4.92 km s^{-1}, (f) 6.94 km s^{-1}.

magnesium sulfate salt. This is because the ability of SEM-EDX analysis to flag stoichiometric compositions of elements requires calibration and careful study. Even with the raw grains, spectra on different grains of the same salt gave a range of relative peak intensities. Furthermore, this identification becomes harder for the impact crater residues. For example, Wozniakiewicz et al. (2009, 2015) have shown that, when using SEM-EDX, in high-speed impacts (6 km s^{-1}), the measured Mg/Si ratios can change depending on several factors (including viewing angle). This is due to self-absorption of X-rays in the samples, which is both energy and path length dependent; this is even before one allows for preferential loss of any elements in the impact data here.

Example spectra from salt crystal-like fragments seen in craters and from melted crater residues are shown in Figs. 7–10. In these figures, example spectra are given from a wide range of impact speeds. Fuller versions of each figure showing the individual spectra separately are given in the supporting information. The presence/absence of various elements in the spectra is summarized in Table 4. The appropriate salt found in each crater can be seen from the spectra and Table 4. One oddity is the appearance of C and O in many of the NaCl impacts. This is unexpected based on projectile composition, but can arise due to contamination of the targets from gun residue. In some case (see the spectra of $MgSO_4$ in Fig. 9), Fe peaks are observed. These may not come from the projectile; it has previously been reported that aluminum foils such as these can contain random inclusions of iron, which if impacted produce iron droplets in the crater residues (e.g., Kearsley et al. 2007; Wozniakiewicz et al. 2015). In general, the lowest speed craters are not fully formed (see Figs. 2–5; Table 2), but in many cases still retain sufficient material to permit an SEM-EDX identification. Thus, as a diagnostic tool, the SEM-EDX has confirmed the presence of projectile material/residue of the appropriate type in the craters over a wide speed range from below 0.5–7 km s^{-1}. However, even at a given speed, the relative heights of peaks in spectra from different craters inside one shot varied, again making a detailed stoichiometric determination difficult. In general, the past work has shown that the detailed stoichiometry of the elements in impact residues is difficult to obtain precisely and requires element-specific corrections. In some cases, it can be done, but is best performed with TEM-EDX and needs corrections against standards to be fully accurate (e.g., see

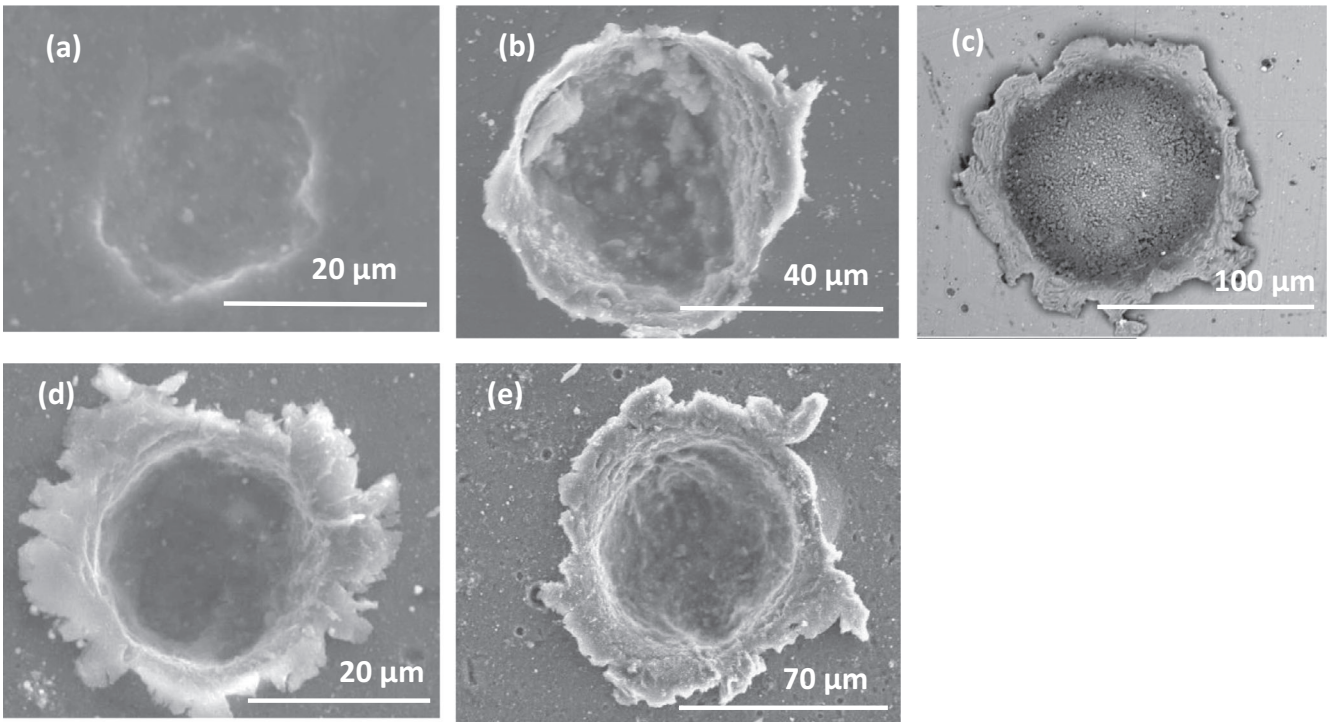

Fig. 4. SEM images showing example impact craters ($MgSO_4$): (a) 0.937 km s^{-1}, (b) 1.99 km s^{-1}, (c) 3.23 km s^{-1}, (d) 5.32 km s^{-1}, (e) 7.34 km s^{-1}.

Wozniakiewicz et al. 2015). However, as shown here, the results from SEM-EDX are sufficient to identify distinct materials.

Raman Analysis

Raman spectroscopy is a powerful tool to identify the presence/absence of the original impacting material in the crater residue. Unfortunately, NaCl does not have a Raman signal, so the technique is only here applied to the other three salts, $NaHCO_3$, $MgSO_4$ (anhydrous), and $MgSO_4{\cdot}7H_2O$. Figure 11 shows spectra from raw grains of all three materials, showing how distinct they are. Figures 12–14 then show spectra at different speeds for $NaHCO_3$, $MgSO_4$ (anhydrous), and $MgSO_4{\cdot}7H_2O$, respectively. When looking at the data, it should be borne in mind that the SEM-EDX results indicated projectile material was present over a wide range of impact speeds.

As can be seen from Fig. 11a, the Raman spectrum from raw $NaHCO_3$ is distinctive and shows the standard peaks (those above 300 cm^{-1} include 650, 684, 1042, 1268, 1436 cm^{-1}) reported in the literature (e.g., Jentzsch et al. 2013). The strongest of these peaks (e.g., 1042 cm^{-1}) are assigned to the HCO_3^- ion. When looking at crater residues versus impact speed (Fig. 12), there was, however, difficulty finding a signal at 0.261 km s^{-1}, indicating that not enough material had been left at the impact site/indentation to respond to the analysis. However, signals were found at 0.499 and 0.931 km s^{-1}, along with the D and G bands of carbon (broad peaks at approximately 1350 and 1578 cm^{-1}, respectively). These carbon bands are a frequent result of gun contamination, so do not necessarily flag carbon from the projectile. At 1.98 km s^{-1}, a transition is seen. The strongest $NaHCO_3$ bands are barely visible in impact residue, even though the SEM-EDX analysis still shows the presence of the elements from the projectile. At higher speeds, no trace of the raw unshocked $NaHCO_3$ spectrum was found in the analysis (see supporting information, e.g., spectra at higher speed).

For $MgSO_4$, the raw Raman spectrum is shown in Fig. 11b, and matches that in the literature (e.g., Wang et al. 2006). There is a strong peak at around 1023 cm^{-1}, with a close neighbor at 1053 cm^{-1}. Both of these are assigned as SO_4 ν_1 vibrational modes. Other strong peaks are seen at 608 and 1123 cm^{-1} (ν_4 and ν_3 modes, respectively). There is also a triplet of peaks, assigned to the ν_2 mode at 451, 475, and 499 cm^{-1}. When spectra from crater residues were studied (Fig. 13), a similar behavior to $NaHCO_3$ was found at low speed; indeed, it was hard to find any trace of the projectile at speeds below 1.99 km s^{-1}. At that speed, however, a strong signal was seen, suggesting that at the lower speeds, insufficient material was retained at the impact site. The strong $MgSO_4$ Raman signal was still

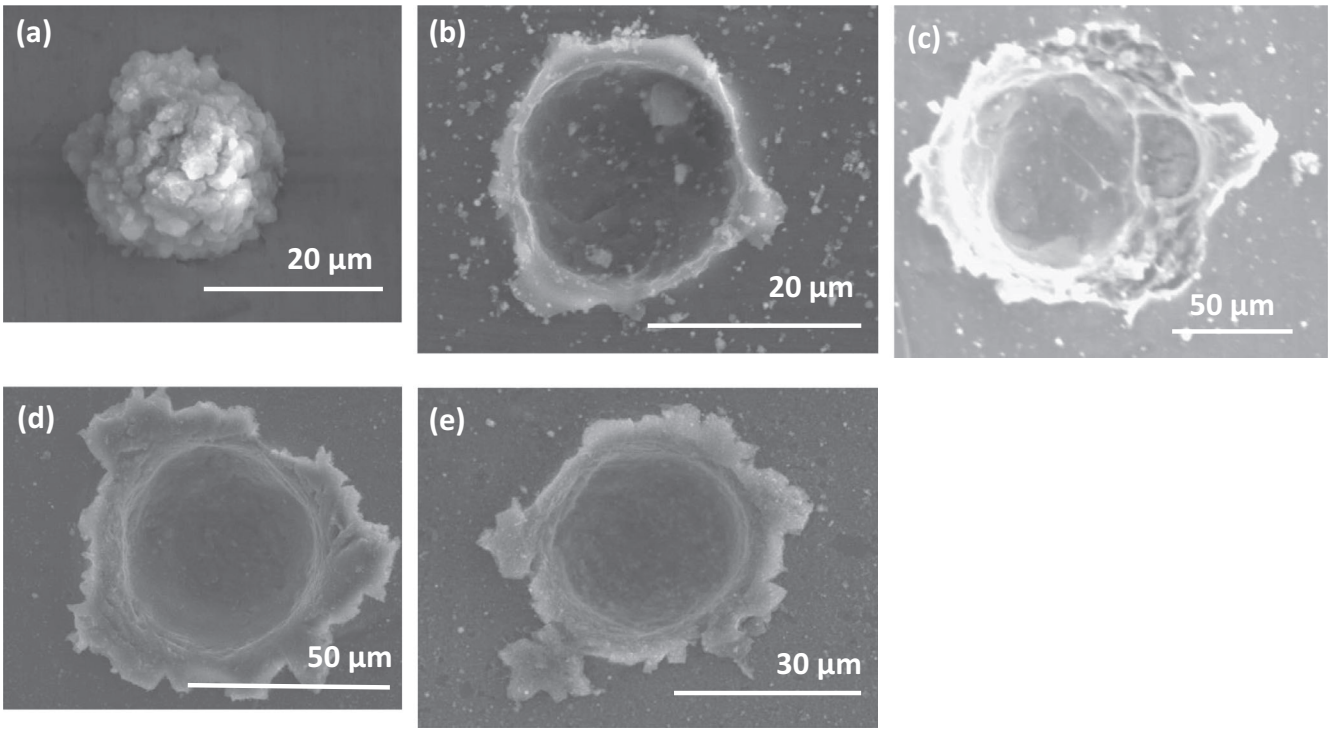

Fig. 5. SEM images showing example impact craters ($MgSO_4 \cdot 7H_2O$): (a) 0.638 km s^{-1}, (b) 2.11 km s^{-1}, (c) 3.29 km s^{-1}, (d) 5.14 km s^{-1}, (e) 7.04 km s^{-1}.

evident at 3.23 km s^{-1}, but was absent at 5.32 km s^{-1} and above (see supporting information, e.g., spectra at higher speed).

The Raman spectrum for raw grains of $MgSO_4 \cdot 7H_2O$ (Fig. 11c) showed the pattern expected for a hydrated magnesium sulfate (e.g., Wang et al. 2006; Jentzsch et al. 2013). Most peaks are again due to the SO_4 vibrational modes. However, the strongest peak (v_1) has shifted from 1023 cm^{-1} to around 983 cm^{-1}, indicating the degree of hydration (see fig. 5 in Wang et al. 2006). A triplet of peaks (v_3) is seen between 1050 and 1135 cm^{-1}, and compared to $MgSO_4$, a distinctive peak is also seen at around 369 cm^{-1}. The results versus impact speed (Fig. 14) showed a similar pattern to those for $MgSO_4$. There were no signals in the low-speed shots, but a strong signal was evident at 2.11 km s^{-1}, with a weak signal at 3.29 km s^{-1}. At 2.11 km s^{-1}, the strong v_1 peak still present at around 983 cm^{-1} indicates that no significant dehydration had occurred in the sample. A weak v_1 signal is still just about visible at a similar place in the spectrum at 3.11 km s^{-1}, indicating that the sample is still not dehydrated. At 5.14 km s^{-1} and above, no Raman signal was present, except the carbon D and G band contamination (see supporting information, e.g., spectra at higher speed).

There is thus a strong contrast in all cases with the SEM-EDX results. There was often insufficient material in the lowest speed impacts to provide a Raman signal. Material with its composition and structure unaltered was, however, present at intermediate speeds. Above a threshold of a few km s^{-1}, however, the Raman signals disappeared, this time indicating that any residue had been altered. The threshold for the Raman signal to vanish was material dependent, being at around 2 km s^{-1} for $NaHCO_3$, and at just above 3 km s^{-1} for $MgSO_4 \cdot 7H_2O$. $MgSO_4$, however, still had a strong Raman signal at 3 km s^{-1}, although this had vanished by 5 km s^{-1}.

Peak Shock Temperatures

We estimated the peak temperature post-shock ($Temp_{ps}$) in NaCl by using the method outlined in Artemieva and Ivanov (2004) and Fritz et al. (2005). The method uses the peak particle velocity in the projectile (u_{max}; obtained here from the PIA) and then determines $Temp_{ps}$ by using:

$$Temp_{ps} = T_0 + [u_{max}^2 - 2E_r]/2C_p, \quad (2)$$

where C_p is the specific heat capacity, and E_r is energy lost from the projectile during release from the shocked state. We obtain E_r from

$$E_r = c/s[u_{max} + c/s \times \ln(c/U_{max})], \quad (3)$$

Table 2. Evolution of crater shape with impact speed. Peak pressures are given for NaCl as found by the planar impact approximation.

Speed (km s^{-1})	Pressure GPa (if NaCl)	Comment
<0.5	<2.8	No real crater, non-circular shallow indentations were observed, some of which held fragments of salt grains. The floors of the indentations were not smooth but had multiple pits.
0.5	2.8	Deeper indentations, with more regular floors, but still non-circular in shape view. Salt grain fragments were often concentrated in the deepest part of the feature.
0.5–1.0	2.8–6.0	Onset of circularity occurs, with thin raised lips around the craters. Distinct grain fragment still line the craters.
1–2	6.0–13.8	More pronounced crater lips appear, with more circular craters. Crater floors show a more melted texture, with projectile residue embedded.
2–3	13.8–23.3	Craters become fully circular. Large crater lips appear, some craters still have distinct fragments of salt grains, and some do not. SEM-EDX shows residue in most craters.
3–4	23.3–34.5	Lips are continuous around the craters but of variable width.
>5	>47.3	Circular craters, with large lips folded over. No obvious crystalline residue, but it was frequently observed with SEM-EDX that melted residue was distributed across the craters.

where c and s for the projectile are as given in Equation 1. Note that this is an approximation and neglects any phase transitions. We have previously used this approach to estimate peak post-shock elevated temperatures in samples of pyrrhotite (Wozniakiewicz et al. 2011). c and s values for NaCl are as given earlier, and we take $C_p = 853$ J kg^{-1} K^{-1}.

The results for the estimates of the peak shock temperatures and the melting point for NaCl at standard pressure are shown in Fig. 15. Based on these estimates, we would expect the onset of melting in the front of the projectile as impact speeds exceed 2 km s^{-1}. The whole projectile could be taken as being shocked to the melting temperature when the rear of the projectile experiences shock pressures similar to those at the front at 2–3 km s^{-1}; this occurs at speeds in excess of 6 km s^{-1} (see Table 3). As stated, the estimates ignore any phase changes, or heating of the rear of the projectile by heat conduction from the front. With these caveats, we note that the results appear to correlate with the disappearance of discrete salt crystal residue above 2 km s^{-1}, with complete melt appearing by 5 km s^{-1}. Given the lack of the appropriate material constants for the other salts, we are not able to repeat these calculations for them.

Table 3. Peak shock pressures for NaCl calculated by the planar impact approximation (PAI) and from the Autodyn hydrocode. The Autodyn hydrocode uses impacts of 60 μm diameter NaCl spheres onto aluminum targets and the pressures are measured at gauge points inside the samples. The front position is close to the point of impact, and the rear the farthest away. This illustrates the drop in peak shock pressure across the bulk of the projectile during an impact.

	PIA	Autodyn		
Velocity (km s^{-1})	Peak pressure GPa	Peak pressure (front) GPa	Peak pressure (middle) GPa	Peak pressure (rear) GPa
0.329	1.74	1.60	0.21	0.025
0.486	2.63	2.47	0.42	0.020
0.954	5.58	5.23	2.05	0.122
2.23	15.5	14.8	9.05	1.12
3.57	29.5	28.4	17.1	4.81
5.03	47.7	46.8	32.1	14.8
6.67	71.0	71.7	53.5	13.0

DISCUSSION

There have been extensive laboratory investigations of survival of mineral projectiles in impacts on metal targets. Many of these studies were at speeds of around 6 km s^{-1}, to support the Stardust mission to comet 81P/Wild-2 (Hörz et al. 2006; Brownlee et al. 2006). Analysis of impact crater residues from the mission itself is summarized in Kearsley et al. (2008) and Price et al. (2010). At an impact speed of 6 km s^{-1}, shock pressures for typical minerals hitting aluminum range from 60 to 90 GPa (Burchell and Kearsley 2009). This is sufficient to alter some minerals, and the issues of resolving pre-impact from postimpact mineralogy is discussed in, among others, Wozniakiewicz et al. (2012). Accordingly, laboratory studies have included shock experiments on materials ranging from phyllosilicates and carbonates (Wozniakiewicz et al. 2015), to more refractory presolar grains (Croat et al. 2015), to study how they survive, or are altered, in impacts at 6 km s^{-1}.

However, at lower speeds, the shock pressures for minerals fall (see Table 5). Although not included in the various minerals used to compile Table 5, the shock pressures for NaCl (Table 3) are in the same range as

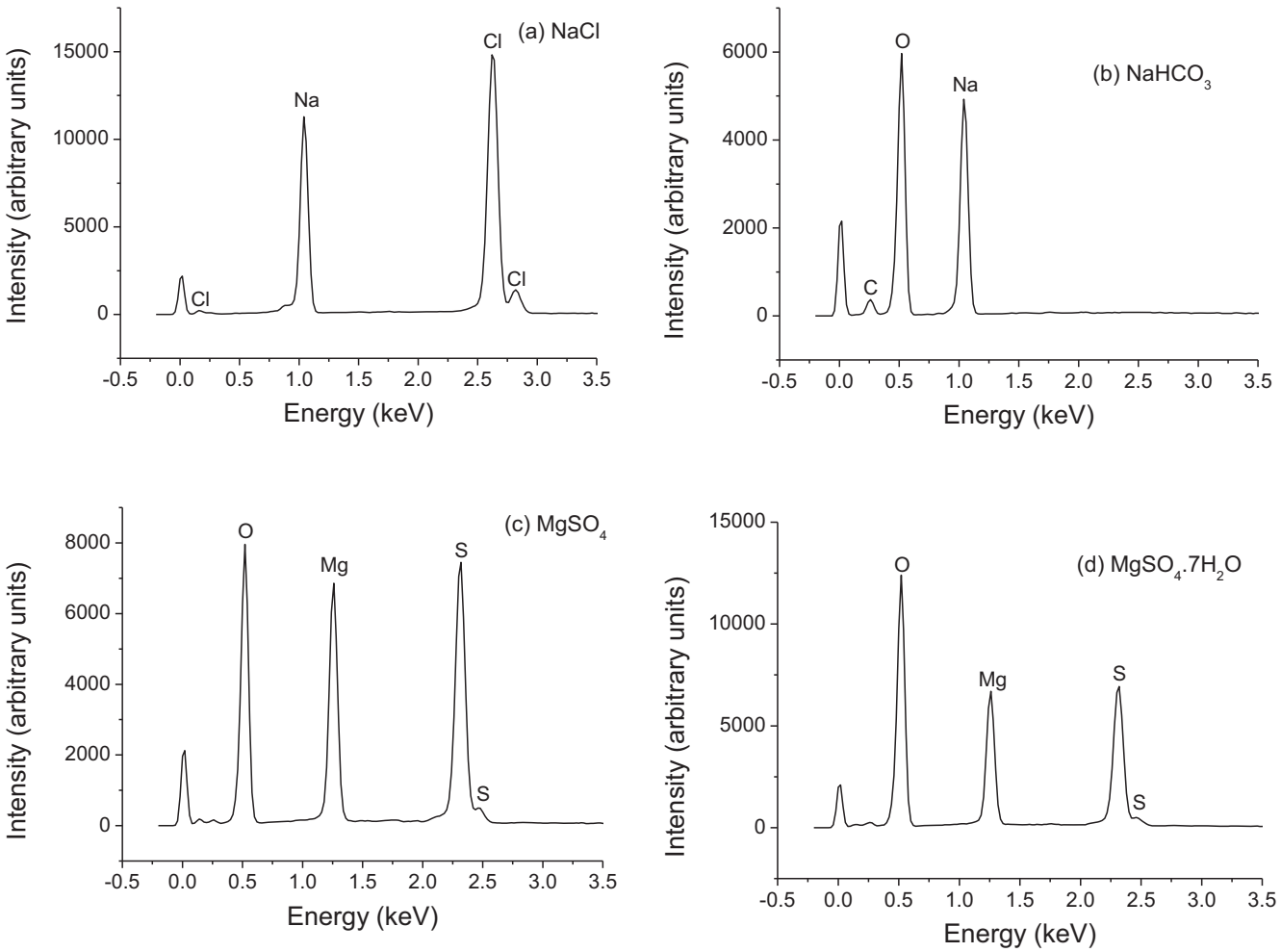

Fig. 6. SEM-EDX spectra of raw grains of (a) NaCl, (b) $NaHCO_3$, (c) $MgSO_4$, and (d) $MgSO_4{\cdot}7H_2O$. The spectra for NaCl, $NaHCO_3$, and $MgSO_4$ are clearly distinct. Those for $MgSO_4$ and $MgSO_4{\cdot}7H_2O$ differ only in the relative magnitude of the oxygen peak at 0.525 keV, with more oxygen seen in the $MgSO_4{\cdot}H_2O$ although this cannot be used to determine exact stoichiometric content without allowance for relative sensitivities between the samples.

Table 4. Peaks present in SEM-EDX spectra of each salt. X indicates observed, – indicates not present, and ~ indicates occasionally observed.

Salt	C	O	Na	Cl	Mg	S
NaCl	~	~	x	x	–	–
$NaHCO_3$	x	x	x	–	–	–
$MgSO_4$	x	x	–	–	x	x
$MgSO_4{\cdot}7H_2O$	x	x	–	–	x	x

those in Table 5 at any given speed. We may thus naively expect that all the salts used here experience pressures in the ranges given in Table 5. It should be noted, however, that for organic materials, shock pressures can be lower. New et al. (2020a), for example, calculate the peak shock pressure of polymethylmethacrylate impacting aluminum at

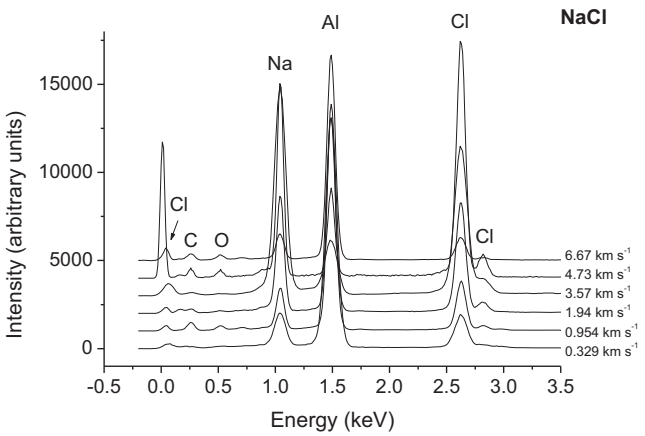

Fig. 7. Example SEM-EDX spectra of crater residues from impacts of grains of NaCl on aluminum foils at differing impact speeds. Strong Na and Cl peaks are seen at all speeds.

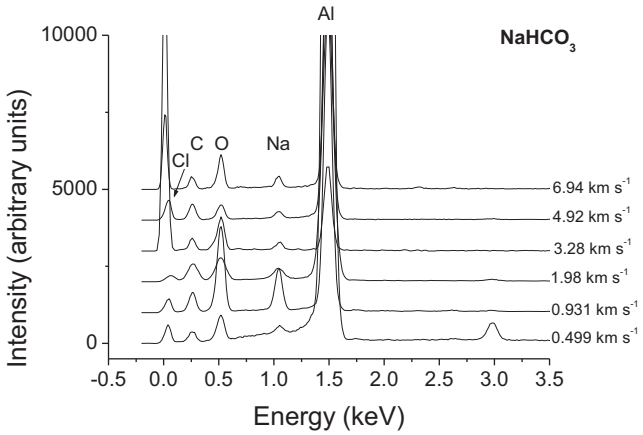

Fig. 8. Example SEM-EDX spectra of crater residues from impacts of grains of $NaHCO_3$ on aluminum foils at differing impact speeds. Na, C, and O peaks are seen at all speeds.

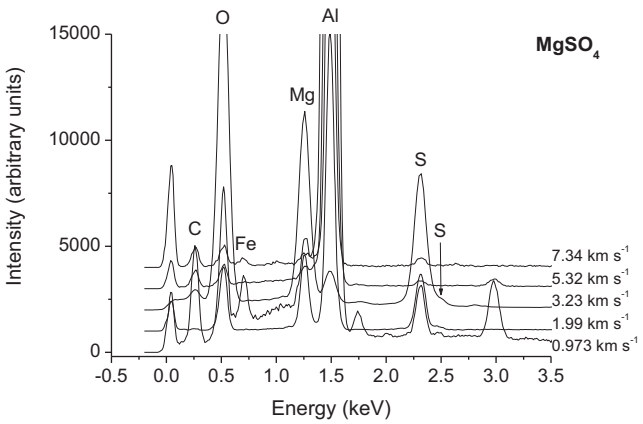

Fig. 9. Example SEM-EDX spectra of crater residues from impacts of grains of $MgSO_4$ on aluminum foils at differing impact speeds. Mg, S, and O peaks are seen at all speeds.

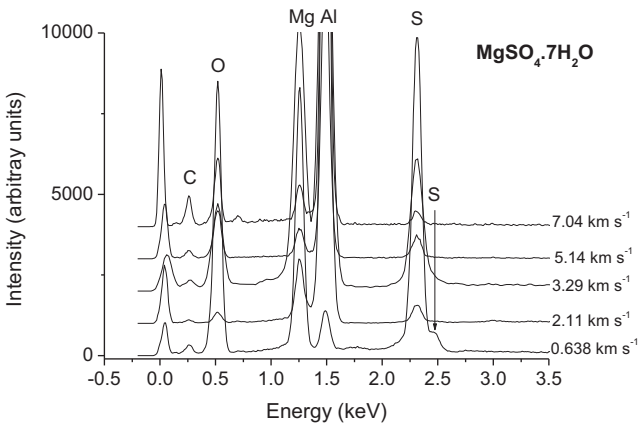

Fig. 10. Example SEM-EDX spectra of crater residues from impacts of grains of $MgSO_4{\cdot}7H_2O$ on aluminum foils at differing impact speeds. Strong Mg, S, and O peaks are seen at all speeds.

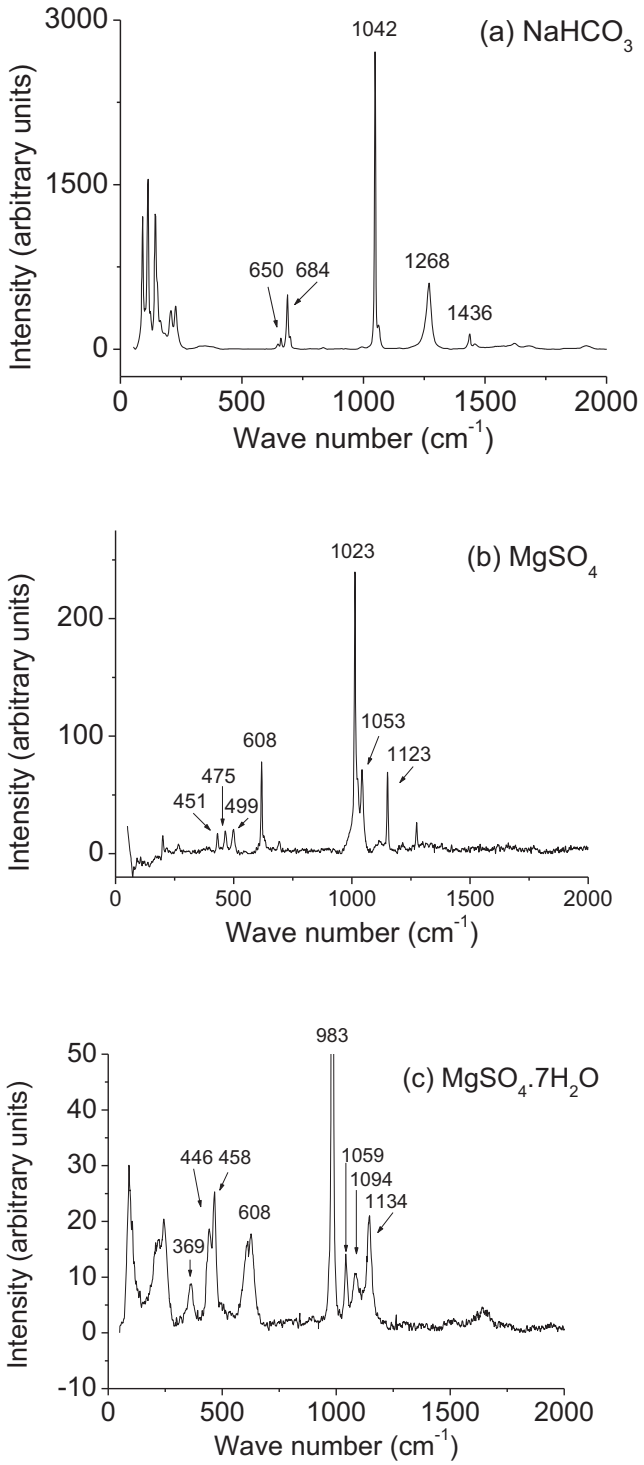

Fig. 11. Raman spectra from raw grains of (a) $NaHCO_3$, (b) $MgSO_4$, and (c) $MgSO_4{\cdot}7H_2O$.

2 km s^{-1}, to be 8.5 GPa, about half that of minerals at the same speed.

From the postshock temperatures calculated for NaCl in Fig. 15, we can see that at between 3 and

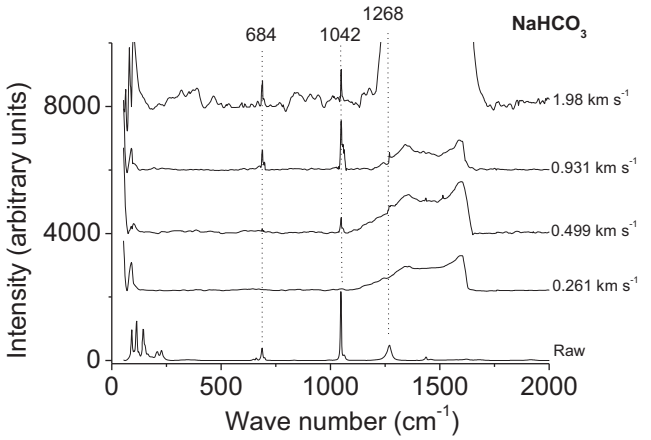

Fig. 12. Raman spectra for crater residues in impacts of $NaHCO_3$ on aluminum foil at various speeds. Spectra from impacts at higher speed are dominated by carbon D and G bands (likely gun contaminants) and show none of the peaks associated with $NaHCO_3$ (see supporting information for more examples).

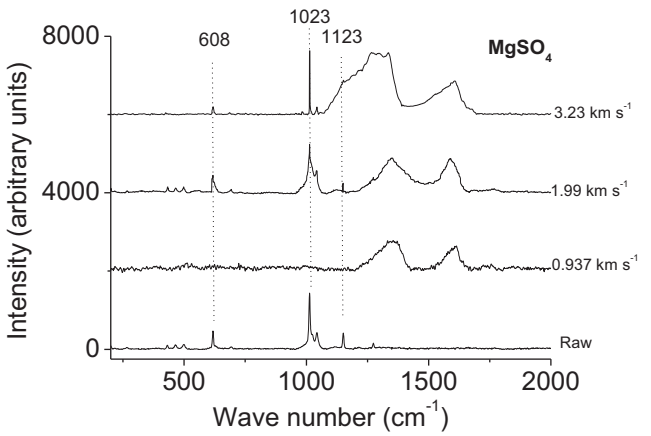

Fig. 13. Raman spectra for crater residues in impacts of $MgSO_4$ on aluminum foil at various speeds. Spectra from impacts at higher speed are dominated by carbon D and G bands (likely gun contaminants) and show none of the peaks associated with $NaHCO_3$ (see supporting information for more examples).

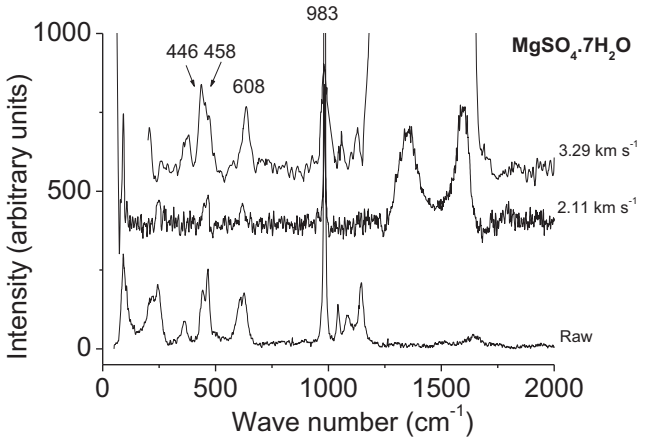

Fig. 14. Raman spectra for crater residues in impacts of $MgSO_4{\cdot}7H_2O$ on aluminum foil at various speeds. Spectra from impacts at higher speed are dominated by carbon D and G bands (likely gun contaminants) and show none of the peaks associated with $NaHCO_3$ (see supporting information for more examples)

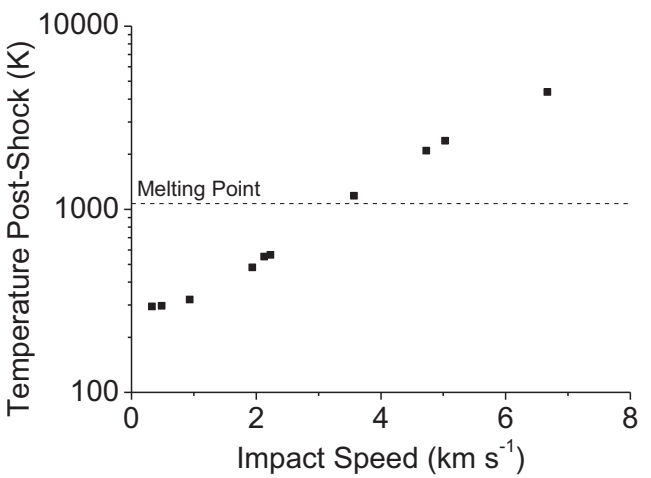

Fig. 15. Post-shock temperatures calculated for NaCl.

4 km s^{-1}, we can expect melting to occur in the bulk of the impactor. Taking this as a proxy for the other salts, we note that this is also the impact speed range where the distinctive Raman spectra of the raw grains disappear from the residues found in the impact craters.

Zhang and Sekine (2007) reported on shock experiments for various salts including $MgSO_4$ and $MgSO_4{\cdot}7H_2O$, at shock pressures up to 36 GPa (equivalent to about 4 km s^{-1} impact speed according to Table 5). They found that while some dehydration was observed at 21–24 GPa (equivalent to about 3 km s^{-1} here), there was no clear evidence for decomposition of $MgSO_4$, even at the highest pressures. This is compatible with the observation here that the Raman spectrum for $MgSO_4{\cdot}7H_2O$ has almost vanished at just above 3 km s^{-1}, but that for $MgSO_4$ is still strong, and only disappears when the impact speed increases further. The Raman signal for $NaHCO_3$, which has a thermal decomposition temperature of 353 K, disappears at an impact speed of about 2 km s^{-1}. All this is broadly in line with the trends of the postshock temperature shown in Fig. 15, but it should be recalled that that graph is for NaCl.

It should be noted that the size of the salt grains used here (75–90 μm) is larger than what will typically be found in a plume of an icy ocean world such as Enceladus or Europa (where grain sizes <20 μm will be

Table 5. Peak impact shock pressures for typical minerals in impacts on aluminum. Adapted from fig. 6 in Burchell and Kearsley (2009).

Impact speed (km s^{-1})	Shock pressure (GPa)
0.5	2–8
1	5–12
2	15–20
3	20–35
4	30–50
5	40–70
6	60–90

more usual). While this will change the absolute quantity of residue available in an individual crater, it will not in itself likely significantly alter the peak shock pressures (and hence temperatures) until grain size falls to around the μm size itself. There, the finite size of the projectile will mean that the strain rate increases above 10^5 s^{-1}. It has been shown that, for some materials, the strength is strain rate dependent and increases sharply above these strain rates, leading to increased shock pressures (see Price et al. 2013). It is not known if the salts used here behave similarly, but it is reasonable to suppose that the present results hold good down to the micron size scale. Furthermore, we note that in a real plume encounter, the grains would not be 100% homogenous particles, so the real peak pressures will be different within each grain due to irregular grain shape, mixing of different materials/voids/crystal dislocations, etc., all of which will modify the peak pressure up or down slightly.

New et al. (2020b) reported that the survival of organics (doped into ice projectiles) when impacting aluminum foils depends on impactor size. Here, we do not determine surviving fraction so cannot compare; a separate future study would be required for that. Furthermore, the data in Fig. 7, New et al. (2020b), show large variability and any new study would have to include larger statistics than here.

CONCLUSIONS

The experimental results presented here show that at typical speeds encountered in orbits or fly-bys of Enceladus and Europa, a range of behaviors are observed. At low impact speeds of a few hundred m s^{-1}, metal collectors suffer rebound of the impactor. This has also been reported for organic impactors by New et al. (2020a). An open box–type collector, with an inclined surface in the interior might be able to focus the incident particles into a collection region. Either that or a sticky surface is required. This is particularly important for even low-altitude orbits of low-mass bodies such as Enceladus, where orbital speeds will be in the range 100–200 m s^{-1}. There are trace residues at the impact sites, which can be detected by SEM-EDX, but there is insufficient material for Raman analysis.

At intermediate speeds of 1 to 2–3 km s^{-1}, impact craters form and retain macroscopic amounts of impacting material. Both SEM-EDX and Raman analysis were able to produce signals. However, while the SEM-EDX analysis could differentiate between general classes of salts (NaCl, $NaHCO_3$, and magnesium sulfates), it could not provide the accurate stoichiometry needed to separate the anhydrous and hydrated states of magnesium sulfate. Raman spectroscopy provided sufficiently distinct spectra that this could be done. Indeed, given that Wang et al. (2006) have shown that the location of the strongest v_1 peak in magnesium sulfates is a good indicator of hydration, this method should be able to distinguish the hydration state of a magnesium sulfate.

At higher speeds (above 3–4 km s^{-1}), and greater shock pressures, the Raman spectra are no longer obtained. However, there is still residue in the impact craters, as indicated by the SEM-EDX analysis. This suggests that shock processing and heating have resulted in impact melt, which no longer retains the crystalline structure necessary for a distinguishable Raman signal.

It should be recalled that these results are for normal incidence impacts. The use of oblique impacts can alter (lower) the peak shock pressures (see Pierazzo and Melosh [2000] for a review of this topic) and thus change the various speed thresholds for residue survival. In addition, the crater shape changes (see Wozniakiewicz et al. [2014], e.g., impacts in aluminum foil similar to that used here) and differing amounts of impactor residue may be retained in a crater as impact angle varies and can be distributed differently around the crater (Daly and Schultz 2018). In a mission to a target such as the plumes of Enceladus or Europa, while the geometry of the fly-through of the plume may suggest a normal (or near-normal) incidence impact, in reality an oblique impact can still be obtained by having an inclined target surface relative to the direction of motion of the space vehicle. Thus, a higher encounter speed can still result in a lower component of the impact speed normal to the target surface, and hence reduced peak shock pressures and potentially higher survival of relatively un-altered residue.

Future experiments firing pure and doped ice at targets (e.g., see Kazemi et al. 2021) hold the prospect of more detailed investigations of what material is retained at impact sites. Finally, we note that these results are for a solid metal target as the collector. If, as advised by Tsou et al. (2012), a different collector material were used, such as aerogel, a highly porous,

low-density medium (see Burchell et al. [2006] for a review of the use of aerogel as a capture medium in space and Brownlee et al. [2006] for its use on the Stardust mission), then semi-intact grains of many materials including organics can be obtained even after impact at 6 km s^{-1}. However, as noted by among others, Chan et al. (2020), the use of aerogels as capture media may not be ideal. To give just one example, the presence of organic solvents in the aerogel manufacturing process (e.g., Sandford et al. 2010) makes detailed organic analysis difficult when looking for weak signals of compounds with simple carbon chemistry. The use of foil collectors as here is thus still highly recommended as suggested, for example, by Mathies et al. (2017).

Acknowledgments—We thank M. Cole and L. Alesbrook for firing the light gas gun. The work in the impact lab was supported by STFC. CF thanks STFC for receipt of a PhD scholarship. K.H. Harris is thanked for useful discussions and support. We thank the referees for useful comments on the manuscript.

Data Availability Statement—Targets are retained in our lab after publication.

Editorial Handling—Dr. Daniel Glavin

REFERENCES

Artemieva N. and Ivanov B. 2004. Launch of Martian meteorites in oblique impacts. *Icarus* 171:84–101.

Bernard R. P. and Hörz F. 1995. Craters in aluminium 1100 by soda-lime glass spheres at 1 to 7 km/s. *International Journal of Impact Engineering* 17:69–80.

Berthoud L., Mandeville J.-C., Durin C., and Borg J. 1995. Debris and meteoroid proportions deduced from impact crater residue analysis. LDEF: 69 months in space. Third Post-Retrieval Symposium, Part 1, pp. 431–444.

Bridges J. C., Burchell M. J., Changela H. C., Foster N. J., Creighton J. A., Carpenter J. D., Gurman S. J., Franchi I. A., and Busemann H. 2010. Iron oxides in comet 81P/Wild 2 samples. *Meteoritics & Planetary Science* 45:55–72.

Brown M. E. and Hand K. P. 2013. Salts and radiation products on the surface of Europa. *Astronomical Journal* 145:110.

Brownlee D., Tsou P., Aleon J., Alexander C. M. O'D., Araki T., Bajt S., Baratta G. A., Bastien R., Bland P., Bleuet P., Borg J., Bradley J. P., Brearley A., Brenker F., Brennan S., Bridges J. C., Browning N. D., Brucato J. R., Bullock E., Burchell M. J., Busemann H., Butterworth A., Chaussidon M., Cheuvront A., Chi M., Cintala M. J., Clark B. C., Clemett S. J., Cody G., Colangeli L., Cooper G., Cordier P., Daghlian C., Dai Z., D'Hendecourt L., Djouadi Z., Dominguez G., Duxbury T., Dworkin J. P., Ebel D. S., Economou T. E., Fakra S., Fairey S. A. J., Fallon S., Ferrini G., Ferroir T., Fleckenstein H., Floss C., Flynn G., Franchi I. A., Fries M., Gainsforth Z., Gallien J.-P., Genge M., Gilles M. K., Gillet P., Gilmour J., Glavin D. P., Gounelle M., Grady M. M., Graham G. A., Grant P. G., Green S. F., Grossemy F., Grossman L., Grossman J. N., Guan Y., Hagiya K., Harvey R., Heck P., Herzog G. F., Hoppe P., Horz F., Huth J., Hutcheon I. D., Ignatyev K., Ishii H., Ito M., Jacob D., Jacobsen C., Jacobsen S., Jones S., Joswiak D., Jurewicz A., Kearsley A. T., Keller L. P., Khodja H., Kilcoyne A.L. D., Kissel J., Krot A., Langenhorst F., Lanzirotti A., Le L., Leshin L. A., Leitner J., Lemelle L., Leroux H., Liu M.-C., Luening K., Lyon I., MacPherson G., Marcus M. A., Marhas K., Marty B., Matrajt G., McKeegan K., Meibom A., Mennella V., Messenger K., Messenger S., Mikouchi T., Mostefaoui S., Nakamura T., Nakano T., Newville M., Nittler L. R., Ohnishi I., Ohsumi K., Okudaira K., Papanastassiou D. A., Palma R., Palumbo M. E., Pepin R. O., Perkins D.,Perronnet M., Pianetta P., Rao W., Rietmeijer F. J. M., Robert F., Rost D., Rotundi A., Ryan R., Sandford S. A., Schwandt C. S., See T. H., Schlutter D., Sheffield-Parker J., Simionovici A., Simon S., Sitnitsky I., Snead C. J., Spencer M. K., Stadermann F. J., Steele A., Stephan T., Stroud R., Susini J., Sutton S. R., Suzuki Y., Taheri M., Taylor S., Teslich N., Tomeoka K., Tomioka N., Toppani A., Trigo-Rodriguez J. M., Troadec D., Tsuchiyama A., Tuzzolino A. J., Tyliszczak T., Uesugi K., Velbel M., Vellenga J., Vicenzi E., Vincze L., Warren J., Weber I., Weisberg M., Westphal A. J., Wirick S., Wooden D., Wopenka B., Wozniakiewicz P., Wright I., Yabuta H., Yano H., Young E. D., Zare R. N., Zega T., Ziegler K., Zimmerman L., Zinner E., and Zolensky M. 2006. Comet 81P/Wild 2 under a microscope. *Science* 314:1711–1716. http://dx.doi.org/10.1126/science.1135840

Bunch T. E., Radicati di Brozolo F., Fleming R. H., Harris D. W., Brownlee D., and Reilly T. W. 1991. LDEF impact craters formed by carbon-rich impactors: A preliminary report. LDEF: 69 months in space. First Post-Retrieval Symposium, Part 1, pp. 549–564.

Burchell M. and Harriss K. 2020. Organic molecules: Is it possible to distinguish aromatics from aliphatics collected by space missions in high speed impacts? *Science* 2:56.

Burchell M. J. and Armes S. P. 2011. Impact ionisation spectra from hypervelocity impacts using aliphatic poly (methyl methacrylate) microparticle projectiles. *Rapid Communications in Mass Spectrometry* 25:543–550.

Burchell M. J. and Kearsley A. T. 2009. Short period Jupiter family comets after Stardust. *Planetary and Space Science* 57:1146–1161.

Burchell M. J., Cole M. J., McDonnell J. A. M., and Zarnecki J. C. 1999. Hypervelocity impact studies using the 2 MV Van de Graaff dust accelerator and two stage light gas gun of the University of Kent at Canterbury. *Measurement Science and Technology* 10:41–50.

Burchell M. J., Graham G., and Kearsley A. 2006. Cosmic dust collection in aerogel. *Annual Reviews of Earth and Planetary Sciences* 34:385–418.

Burchell M. J., Foster N. J., Kearsley A. T., and Creighton J. A. 2008. Identification of mineral impactors in hypervelocity impact craters in aluminium by Raman spectroscopy of residues. *Meteoritics & Planetary Science* 43:135–142.

Carr M. H., Belton M. J. S., Chapman C. R., Davies A. S., Geissler P., Greenberg R., McEwen A. S., Tufts B. R., Greeley R., Sullivan R., Head J. W., Pappalardo R. T., Klaasen K. P., Johnson T. V., Kaufman J., Senske D., Moore J., Neukum G., Schubert G., Burns J. A., Thomas

P., and Veverka J. 1998. Evidence for a subsurface ocean on Europa. *Nature* 391:363–365.

Chan D. H., Millet A., Fisher C. R., Price M. C., Burchell M. J., and Armes S. P. 2021. Synthesis and characterization of polypyrrole-coated anthracene microparticles: A new synthetic mimic for polyaromatic hydrocarbon-based cosmic dust. *ACS Applied Materials & Interfaces* 13:3175–3185.

Chan Q. H. S., Stroud R., Martins Z., and Yabuta H. 2020. Concerns of organic contamination for sample return space missions. *Space Science Reviews* 216:56.

Croat T. K., Floss C., Haas B. A., Burchell M. J., and Kearsley A. T. 2015. Survival of refractory presolar grain analogs during Stardust-like impact into Al foils: Implications for Wild 2 presolar grain abundances and study of the cometary fine-fraction. *Meteoritics & Planetary Science* 50:1378–1391.

Daly T. R. and Schultz P. 2018. Projectile preservation during oblique hypervelocity impacts. *Meteoritics & Planetary Science* 53:1364–1390.

Dougherty M. K., Khurana K. K., Neubauer F. M., Russell C. T., Saur J., Leisner J. S., and Burton M. E. 2006. Identification of a dynamic atmosphere at Enceladus with the Cassini magnetometer. *Science* 311:1406–1409.

Foster N. F., Wozniakiewicz P. J., Price M. C., Kearsley A. T., and Burchell M. J. 2013. Identification of Mg–Fe content of olivine samples (by Raman spectroscopy) after impact at 6 km s^{-1} onto aluminium foil and aerogel: In the laboratory and in Wild-2 cometary samples returned by Stardust. *Cosmochimica et Geochimica Acta* 121:1–14.

Fritz J., Artemieva N., and Greshake A. 2005. Ejection of Martian meteorites. *Meteoritics & Planetary Science* 40:1393–1411.

Fritz J. N., Marsh S. P., Carter W. J., and McQueen R. G. 1971. The Hugoniot equation of state of sodium chloride in the sodium chloride structure. Proceedings National Bureau of Standards Symposium, Gaithersburg, Maryland (1968). *NBS Special Publications* 326:201–208.

Goldsworthy B. J., Burchell M. J., Cole M. J., Green S. F., Leese M. R., McBride N., McDonnell J. A. M., Müller M., Grün E., Srama R., Armes S. P., and Khan M. A. 2002. Laboratory calibration of the Cassini Cosmic Dust Analyser (CDA) using new, low density projectiles. *Advances in Space Research* 29:1139–1144.

Goldsworthy B. J., Burchell M. J., Cole M. J., Armes S. P., Khan M. A., Lascelles S. F., Green S. F., McDonnell J. A. M., Srama R., and Bigger S. W. 2003. Time of flight mass spectra of ions in plasmas produced by hypervelocity impacts of organic and mineralogical microparticles on a cosmic dust analyser. *Astronomy & Astrophysics* 409:1151–1167.

Grasset O., Castillo-Rogez J., Guillot T., Fletcher L. N., and Tosi F. 2017. Water and volatiles in the outer solar system. *Space Science Reviews* 212:835–875.

Guzman M., Lorenz R., Hurley D., Farrell W., Spencer J., Hansen C., Hurford T., Ibea J., Carlson P., and McKay C. P. 2019. Collecting amino acids in the Enceladus plume. *International Journal of Astrobiology* 18:47–59.

Hand K. P. and Carlson R. W. 2015. Europa's surface color suggests an ocean rich with sodium chloride. *Geophysical Research Letters* 42:3174–3178.

Hansen C., Esposito L., Stewart A. I. F., Colwell J., Hendrix A., Pryor W., Shemansky D., and West R. 2006. Enceladus' water vapor plume. *Science* 311:1422–1426.

Hayhurst C. J. and Clegg R. A. 1987. Cylindrically symmetric SPH simulations of hyper- velocity impacts on thin plates. *International Journal of Impact Engineering* 20:337–348.

Hendrix A. R., Hurford T. A., Barge L. M., Bland M. T., Bowman J. S., Brinckerhoff W., Buratti B. J., Cable M. L., Castillo-Rogez J., Collins G. C., Diniega S., German C. R., Hayes A. G., Hoehler T., Hosseini S., Howett C. J. A., McEwen A. S., Neish C. D., Neveu M., Nordheim T. A., Patterson G. W., Patthoff D. A., Phillips C., Rhoden A., Schmidt B. E., Singer K. N., Soderblom J. M., and Vance S. D. 2019. The NASA roadmap to ocean worlds. *Astrobiology* 19:1–27.

Hibbert R. H., Cole M. J., Price M. C., and Burchell M. J. 2017. The hypervelocity impact facility at the University of Kent: Recent upgrades and specialised facilities. *Procedia Engineering* 204:208–214.

Horz F., Bastien R., Borg J., Bradley J. P., Bridges J. C., Brownlee D. E., Burchell M. J., Chi M., Cintala M. J., Dai Z. R., Djouadi Z., Dominguez G., Economou T. E., Fairey S. A. J., Floss C., Franchi I. A., Graham G. A., Green S. F., Heck P., Hoppe P., Huth J., Ishii H., Kearsley A. T., Kissel J., Leitner J., Leroux H., Marhas K., Messenger K., Schwandt C. S., See T. H., Snead C., Stadermann F. J., Stephan T., Stroud R., Teslich N., Trigo-Rodriguez J. M., Tuzzolino A. J., Troadec D., Tsou P., Warren J., Westphal A., Wozniakiewicz P., Wright I., and Zinner E. 2006. Impact features on stardust: Implications for comet 81P/Wild 2 dust. *Science* 314:1716–1719. http://doi.org/10.1126/science.1135705

Jentzsch P. V., Kampe B., Ciobotă V., Rösch P., and Popp J. 2013. Inorganic salts in atmospheric particulate matter: Raman spectroscopy as an analytics took. *Spectrochimica Acta Part A: Molecular and Biomolecular Spectroscopy* 115:697–708.

Kazemi B., New J. S., Golozar M., Casto L. D., Butterworth A. L., and Mathies R. A. 2021. Method for detecting and quantitating capture of organic molecules in hypervelocity impacts. *MethodsX* 8:101239.

Kearsley A. T., Graham G. A., Burchell M. J., Cole M. J., Dai Z. R., Teslich N., Bradley J. P., Chater R., Wozniakiewicz P. J., Spratt J., and Jones G. 2007. Analytical scanning and transmission electron microscopy of laboratory impacts on Stardust aluminium foils: Interpreting impact crater morphology and the composition of impact residues. *Meteoritics & Planetary Science* 42:191–210.

Kearsley A. T., Borg J., Graham G. A., Burchell M. J., Cole M. J., Leroux H., Bridges J. C., Hörz F., Wozniakiewicz P. J., Bland P. A., Bradley J. P., Dai Z. R., Teslich N., See T., Hoppe P., Heck P. R., Huth J., Stadermann F. J., Floss C., Marhas K., Stephan T., and Leitner J. 2008. Dust from comet Wild 2: Interpreting particle size, shape, structure and composition from impact features on the Stardust aluminium foils. *Meteoritics & Planetary Science* 43:41–74.

Khawaja N., Postberg F., Hillier J., Klenner F., Kempf S., Nölle L., Reviol L. R., Zou Z., and Srama R. 2019. Low mass nitrogen-, oxygen-bearing, and aromatic compounds in Enceladean ice grains. *Monthly Notices of the Royal Astronomical Society* 489:5231–5243.

Khurana K. K., Kivelson M. G., Stevenson D. J., Schubert G., Russell C. T., Walker R. J., and Polanskey C. 1998. Induced magnetic fields as evidence for subsurface oceans in Europa and Callisto. *Nature* 395:777–780.

Lorenz R. D. 2016. Europa ocean sampling by plume flythrough: Astrobiological expectations. *Icarus* 267:217–219.

Marsh S. P. 1980. *LASL shock Hugoniot data*. Los Angeles: University of California Press. 674 p.

Mathies R. A., Razu M. E., Kim J., Stockton A. M., Turin P., and Butterworth A. 2017. Feasibility of detecting bioorganic compounds in Enceladus plumes with the Enceladus Organic Analyzer. *Astrobiology* 17:902–912.

Melosh H. J. 2013. Contact and compression stage of impact cratering. In *Impact cratering processes and products*, edited by Osinski G. R. and Pierazzo E. Chichester, UK: Wiley-Blackwell. pp. 32–42.

Moral A. G., Rull F., Maurice S., Hutchinson I. B., Canora C. P., Seoane L., López-Reyes G., Rodriguez Prieto J. A., Rodríguez P., Ramos G., Parot Y., and Forni O. 2020. Design, development and scientific performance of the Raman Laser Spectrometer EQM on the 2020 Exomars (ESA) Mission. *Journal of Raman Spectroscopy* 51:1771–1781.

New J. S., Mathies R. A., Price M. C., Cole M. J., Golozar M., Spathis V., Burchell M. J., and Butterworth A. L. 2020a. Characterizing organic particle hypervelocity impacts on inert metal surfaces: Foundations for capturing organic molecules in hypervelocity transits of Enceladus plumes. *Meteoritics & Planetary Science* 55:465–479.

New J. S., Kazemi B., Price M. C., Cole M. J., Spathis V., Mathies R. A., and Butterworth A. L. 2020b. Feasibility of Enceladus plume biosignature analysis: Successful capture of organic ice particles in hypervelocity impacts. *Meteoritics & Planetary Science* 55:1936–1948.

Nimmo F., Spencer J. R., Pappalardo R. T., and Mullen M. E. 2007. Shear heating as the origin of the plumes and heat flux on Enceladus. *Nature* 447:289–291.

Pappalardo R. T., Belton M. J. S., Breneman H. H., Carr M. H., Chapman C. R., Collins G. C., Denk T., Fagents S., Geissler P. E., Giese B., Greeley R., Greenberg R., Head J. W., Helfenstein P., Hoppa G., Kadel S. D., Klaasen K. P., Klemaszewski J. E., Magee K., McEwen A. S., Moore J. M., Moore W. B., Neukum G., Phillips C. B., Prockter L. M., Schubert G., Senske D. A., Sullivan R. J., Tufts B. R., Turtle E. P., Wagner R., and Williams K. K. 1999. Does Europa have a subsurface ocean? Evaluation of the geological evidence. *Journal of Geophysical Research-Planets* 104:24,015–24,055.

Pierazzo E. and Melosh H. J. 2000. Understanding oblique impacts from experiments, observations and modeling. *Annual Review of Earth and Planetary Sciences* 28:141–167.

Porco C. C., Helfenstein P., Thomas P. C., Ingersoll A. P., Wisdom J., West R., Neukum G., Denk T., Wagner R., Roatsch T., Kieffer S., Turtle E., McEwen A., Johnson T. V., Rathbun J., Veverka J., Wilson D., Perry J., Spitale J., Brahic A., Burns J. A., DelGenio A. D., Dones L., Murray C. D., and Squyres S. 2006. Cassini observes the active south pole of Enceladus. *Science* 311:1393–1401.

Postberg F., Kempf S., Schmidt J., Brilliantov N., Beinsen A., Abel B., Buck U., and Srama R. 2009. Sodium salts in E ring ice grains from an ocean below the surface of Enceladus. *Nature* 459:1098–2001.

Postberg F., Schmidt J., Hillier J., Kempf S., and Srama R. 2011. A salt-water reservoir as the source of a compositionally stratified plume on Enceladus. *Nature* 474:620–622.

Postberg F., Khawaja N., Abel B., Choblet G., Glein C. R., Gudipati M. S., Henderson B. L., Hsu H. W., Kempf S., Klenner F., Moragas-Klostermeyer G., Magee B., Nölle L., Perry M., Reviol R., Schmidt J., Srama R., Stolz F., Tobie G., Trieloff M., and Waite J. H. 2018. Macromolecular organic compounds from the depths of Enceladus. *Nature* 558:564–567.

Price M. C., Kearsley A. T., Burchell M. J., Hörz F., Borg J., Bridges J. C., Cole M. J., Floss C., Graham G., Green S. F., Hoppe P., Leroux H., Marhas K. K., Park N., Stroud R., Stadermann F. J., and Wozniakiewicz P. J. 2010. Comet 81P/Wild 2: The size distribution of finer (sub 10 micrometre) dust collected by the Stardust spacecraft. *Meteoritics & Planetary Science* 45:1409–1428.

Price M. C., Kearsley A. T., and Burchell M. J. 2013. Validation of the Preston-Tonks-Wallace strength model at strain rates of 10^{13} s^{-1} for Al-1100, tantalum and copper using hypervelocity impact crater morphologies. *International Journal of Impact Engineering* 52:1–10.

Roth L., Saur J., Retherford K. D., Strobel D. F., Feldman P. D., McGrath M. A., and Nimmo F. 2014. Transient water vapor at Europa's south pole. *Science* 343:171–174.

Sandford S. A., Bajt S., Clemett S. J., Cody G. D., Cooper G., Degregorio B. T., de Vera V., Dworkin J. P., Elsila J. E., and Flynn G. J. 2010. Assessment and control of organic and other contaminants associated with the Stardust sample return from comet 81P/Wild 2. *Meteoritics & Planetary Science* 45:406–433.

Sohl F., Choukroun M., Kargel J., Kimura J., Pappalardo R., Vance S., and Zolotov M. 2010. Subsurface water oceans on icy satellites: Chemical composition and exchange processes. *Space Science Reviews* 153:485–510.

Southworth B. S., Kempf S., and Schmidt J. 2015. Modeling Europa's dust plumes. *Geophysical Research Letters* 42:10,541–10,548.

Spahn F., Schmidt J., Albers N., Hörning M., Makuch M., Seiß M., Kempf S., Srama R., Dikarev V., Helfert S., Moragas-Klostermeyer G., Krivov A. V., Sremcevic M., Tuzzolino A. J., Economou T., and Grün E. 2006. Cassini dust measurements at Enceladus and implications for the origin of the E ring. *Science* 311:1416–1418.

Sparks W. B., Hand K. P., McGrath M. A., Bergeron E., Cracraft M., and Deustua S. E. 2016. Probing for evidence of plumes on Europa with HST/STIS. *The Astrophysical Journal* 829:121.

Srama R., Ahrens T. J., Altobelli N., Auer S., Bradley J. G., Burton M., Dikarev V. V., Economou T., Fechtig H., Görlich M., Grande M., Graps A., Grün E., Havnes O., Helfert S., Horanyi M., Igenbergs E., Jessberger E. K., Johnson T. V., Kempf S., Krivov A. V., Krüger H., Mocker-Ahlreep A., Moragas-Klostermeyer G., Lamy P., Landgraf M., Linkert D., Linkert G., Lura F., McDonnell J. A. M., Möhlmann D., Morfill G. E., Müller M., Roy M., Schäfer G., Schlotzhauer G., Schwehm G. H., Spahn F., Stübig M., Svestka J., Tschernjawski V., Tuzzolino A. J., Wäsch R., and Zook H. A. 2004. The Cassini Cosmic Dust Analyzer. *Space Science Reviews* 114:465–518.

Traspas A. and Burchell M. J. 2021. Tardigrade survival limits in high speed impacts—Implications for Panspermia and collection of samples from plumes emitted by ice worlds. *Astrobiology* 21:845–852.

Tsou P., Brownlee D. E., McKay C. E., Anbar A. D., Yano H., Altwegg K., Beegle L. W., Dissly R., Strange N. J., and Kanik I. 2012. LIFE: Life investigation for Enceladus

a sample return mission concept in search for evidence of life. *Astrobiology* 12:730–742.

Waite J. H., Combi M. R., Ip W. H., Cravens T. E., McNutt R. L., Kasprzak W., Yelle R., Luhmann J., Niemann H., Gell D., Magee B., Fletcher G., Lunine J., and Tseng W. L. 2006. Cassini ion and neutral mass spectrometer: Enceladus plume composition and structure. *Science* 311:1419–1422.

Wang A., Freeman J. F., Joliffe B. L., and Chou I. M. 2006. Sulfates on Mars: A systematic Raman spectroscopic study of hydration states of magnesium sulfates. *Geochimica et Cosmochimica Acta* 70:6118–6135.

Wiens R. C., Maurice S., Robinson S. H., Nelson A. E., Cais P., Bernardi P., Newell R. T., Clegg S., Sharma S. K., Storms S., Deming J., Beckman D., Ollila A. M., Gasnault O., Anderson R. B., André Y., Michael Angel S., Arana G., Auden E., Beck P., Becker J., Benzerara K., Bernard S., Beyssac O., Borges L., Bousquet B., Boyd K., Caffrey M., Carlson J., Castro K., Celis J., Chide B., Clark K., Cloutis E., Cordoba E. C., Cousin A., Dale M., Deflores L., Delapp D., Deleuze M., Dirmyer M., Donny C., Dromart G., George Duran M., Egan M., Ervin J., Fabre C., Fau A., Fischer W., Forni O., Fouchet T., Fresquez R., Frydenvang J., Gasway D., Gontijo I., Grotzinger J., Jacob X., Jacquinod S., Johnson J. R., Klisiewicz R. A., Lake J., Lanza N., Laserna J., Lasue J., Le Mouélic S., Legett C., Leveille R., Lewin E., Lopez-Reyes G., Lorenz R., Lorigny E., Love S. P., Lucero B., Madariaga J. M., Madsen M., Madsen S., Mangold N., Manrique J. A., Martinez J. p., Martinez-Frias J., McCabe K. P., McConnochie T. H., McGlown J. M., McLennan S. M., Melikechi N., Meslin P.-Y., Michel J. M., Mimoun D., Misra A., Montagnac G., Montmessin F., Mousset V., Murdoch N., Newsom H., Ott L. A., Ousnamer Z. R., Pares L., Parot Y., Pawluczyk R., Glen Peterson C., Pilleri P., Pinet P., Pont G., Poulet F., Provost C., Quertier B., Quinn H., Rapin W., Reess J.-M., Regan A. H., Reyes-Newell A. L., Romano P. J., Royer C., Rull F., Sandoval B., Sarrao J. H., Sautter V., Schoppers M. J., Schröder S., Seitz D., Shepherd T., Sobron P., Dubois B., Sridhar V., Toplis M. J., Torre-Fdez I., Trettel I. A., Underwood M., Valdez A., Valdez J., Venhaus D., and Willis P. 2021. The SuperCam Instrument Suite on the NASA Mars 2020 Rover: Body unit and combined system tests. *Space Science Reviews* 217:4.

Wozniakiewicz P. J., Kearsley A. T., Burchell M. J., Foster N. J., Cole M. J., Bland P. A., and Russell S. S. 2009. Analysis of residues resulting from laboratory impacts into aluminum 1100 foil: Implications for Stardust crater analyses. *Meteoritics & Planetary Science* 44:1541–1559.

Wozniakiewicz P. J., Ishii H. A., Kearsley A. T., Burchell M. J., Bland P. A., Bradley J. P., Dai Z., Teslich N., Collins G. S., Cole M. J., and Russell S. S. 2011. Investigation of iron sulphide impact crater residues: A combined analysis by scanning and transmission electron microscopy. *Meteoritics & Planetary Science* 46:1007–1024.

Wozniakiewicz P. J., Ishii H. A., Kearsley A. T., Burchell M. J., Bradley J. P., Price M. C., Teslich N., Lee M. R., and Cole M. J. 2012. Stardust impact analogues: resolving pre- and post-impact mineralogy in Stardust Al foils. *Meteoritics & Planetary Science* 47:708–728.

Wozniakiewicz P. J., Price M. C., Armes S. P., Burchell M. J., Cole M. J., Fielding L. A., Hillier J. K., and Lovett J. R. 2014. Micron-scale hypervelocity impact craters: Dependence of crater ellipticity on impact trajectory, projectile size, velocity and shape. *Meteoritics & Planetary Science* 49:1929–1947.

Wozniakiewicz P. J., Ishii H. A., Kearsley A. T., Bradley J. P., Price M. C., Burchell M. J., Teslich N., and Cole M. J. 2015. The survivability of phyllosilicates and carbonates impacting Stardust Al foils: Facilitating the search for cometary water. *Meteoritics & Planetary Science* 50:2003–2023.

Zhang F. and Sekine T. 2007. Impact-shock behavior of Mg- and Ca-sulfates and their hydrates. *Geochimica et Cosmochimica Acta* 71:4125–4133.

SUPPORTING INFORMATION

Additional supporting information may be found in the online version of this article.

Fig. S1. SEM-EDX spectra from example NaCl impacts. Impact speeds of (a) 0.329 km s^{-1}, (b) 0.954 km s^{-1}, (c) 1.94 km s^{-1} (d) 3.57 km s^{-1} (e) 4.73 km s^{-1}, and (f) 6.67 km s^{-1}.

Fig. S2. SEM-EDX spectra from example $NaHCO_3$ impacts. Impact speeds of (a) 0.499 km s^{-1} (b) 0.931 km s^{-1}, (c) 1.98 km s^{-1}, (d) 3.28 km s^{-1} (e) 4.92 km s^{-1}, and (f) 6.94 km s^{-1}.

Fig. S3. SEM-EDX spectra from example $MgSO_4$ impacts. Impact speeds of (a) 0.937 km s^{-1}, (b) 1.99 km s^{-1}, (c) 3.23 km s^{-1}, (d) 5.32 km s^{-1} and (e) 7.34 km s^{-1}.

Fig. S4. SEM-EDX spectra from example $MgSO_4 \cdot 7H_2O$ impacts. Impact speeds of (a) 0.638 km s^{-1}, (b) 2.11 km s^{-1}, (c) 3.29 km s^{-1}, (d) 5.14 km s^{-1}, and (e) 7.04 km s^{-1}.

Fig. S5. Raman spectra for $NaHCO_3$ (a) Raw grain, and crater residues with impact speed (b) 0.261 km s^{-1}, (c) 0.499 km s^{-1}, (d) 0.931 km s^{-1}, (e) 1.98 km s^{-1}, (f) 3.28 km s^{-1} (g) 4.92 km s^{-1}, and (g) 6.94 km s^{-1}.

Fig. S6. Raman spectra for $MgSO_4$ (a) Raw grain, and crater residues with impact speed (b) 0.937 km s^{-1}, (c) 1.99 km s^{-1}, (d) 3.23 km s^{-1}, (e) 5.32 km s^{-1}, and (f) 7.34 km s^{-1}.

Fig. S7. Raman spectra for $MgSO_4 \bullet 7H_2O$ (a) Raw grain, and crater residues with impact speed (b) 2.11 km s^{-1}, (c) 3.29 km s^{-1}, (d) 5.14 km s^{-1}, and (e) 7.14 km s^{-1}.